PHYSICAL REVIEW B **86**, 155455 (2012)

Magnetic configuration, electronic structure, and stability of the low-index surfaces of η-Mn_3N_2: A first-principles study

Andrzej Kędziorski[1,2] and M. Carmen Muñoz[1,*]

[1] *Instituto de Ciencia de Materiales de Madrid, Consejo Superior de Investigaciones Científicas, (ICMM-CSIC), Cantoblanco, E-28049 Madrid, Spain*

[2] *Institute of Physics, Nicolaus Copernicus University, PL-Toruń, Poland*

(Received 30 July 2012; published 31 October 2012)

The low-index (001), (010), and (110) surfaces of η-Mn_3N_2 are investigated using the *ab initio* generalized gradient (GGA) density functional method. For the bulk crystal, the GGA approach is found to predict correctly its electronic structure and the antiferromagnetic ordering along the [001] direction, with Mn magnetic moments close to $3\mu_B$. The more stable surfaces are the (001) terminated in a MnN plane and the (010), both observed experimentally in η-Mn_3N_2 thin films grown on MgO (001) crystals. While in the (001) the surface plane consists of Mn atoms ferromagnetically coupled through N, in the (010) surface rows of Mn antiferromagnetically aligned alternate along the [001] direction. Furthermore, our results suggest that, due to its relatively small surface energy, the (110) surface with a singular one-dimensional ribbonlike 8.46 Å width ferromagnetic structure could also be stabilized. Despite their differences, the magnetic configuration of all the surfaces is dictated by the cleavage of the layerwise antiferromagnetic structure of bulk Mn_3N_2. The broken symmetry of the surface induces atomic corrugations, which however do not alter drastically either the spin configuration or the electronic structure. Mn-N bond states tend to be close to the bottom of the valence bands, and although an enhancement of the surface magnetic moments are obtained, they remain close to the bulk values. All the surfaces are metallic as bulk η-Mn_3N_2 crystals.

DOI: 10.1103/PhysRevB.86.155455 PACS number(s): 71.20.−b, 75.70.Rf, 31.15.A−

I. INTRODUCTION

Manganese nitrides exhibit unique structural and spin configurations among transition-metal compounds. They are interesting and attractive magnetic materials offering variable phase-dependent structural and magnetic properties. They differ on the nitrogen content and range from the antiferromagnetic θ-MnN to the ϵ-Mn_4N ferrimagnetic phase.[1–4] Mn nitrides also have interest in the field of dilute magnetic semiconductors. It was first suggested that Mn clusters were responsible for ferromagnetism in Mn doped GaN[5], although recently it has been proposed that a segregated Mn_4N phase may account for the observed ferromagnetism.[6] Furthermore, the formation of a distorted Mn_3N_2 phase at the interface of Mn/Si_3N_4 multilayers, has been invoked to explain the weak-ferromagnetic behavior presented by the multilayers.[7,8] Among all the manganese nitrides, the η-Mn_3N_2 phase is known to be antiferromagnetic (AFM) with a reported Nèel temperature of 925 K.[2,4,9] Its structure is a slightly distorted face-centered tetragonal rock salt with two layers of MnN separated by a layer of Mn along the c axis. Neutron scattering measurements have shown that in bulk Mn_3N_2, the Mn magnetic moments are aligned ferromagnetically within the planes and alternate antiferromagnetically in consecutive planes along the c axis. Thin films of Mn_3N_2 grown on MgO (001) by molecular beam epitaxy, also present antiferromagnetism[10,11] and atomic-scale spin-polarized scanning tunneling microscopy of the corresponding (010) surface has revealed that the AFM order remains at the surface.[12–17] In addition, the Mn tetramer cluster has also been recently stabilized at the (001) face of Mn_3N_2.[18]

Previous first-principles electronic structure calculations, within the local spin density functional approximation (LSDA-DFT), show a good agreement with the AFM ordering measured experimentally in bulk MnN and Mn_3N_2, provided the experimental unit cell volumes are used in the calculation. However, for the MnN fully relaxed structure the LSDA approach predicts a ferromagnetic ground state.[19] Therefore, spin configuration and bond lengths seem to be intimately linked and determinant to establish the magnetic ground state. Furthermore, both, LSDA[14] and GGA[17] calculations have been performed for (010) Mn_3N_2 thin films using the experimental bulk geometry. In agreement with the scanning tunneling microscopy results, an undistorted AFM surface is found, but to our knowledge the study of the magnetic structure of relaxed slabs has not been attempted. In this paper we investigate the energy, spin configuration, and magnetic properties of the low-index surfaces of face-centered tetragonal Mn_3N_2 crystals. Since the final spin configuration in Mn_3N_2 is due to a delicate balance of ferro- and antiferromagnetic exchange interactions, which in turns depend on bond lengths and bond angles, the dependence of the bulk magnetic configuration on the interatomic distances and lattice parameters are first explored theoretically. Furthermore, the effect of the structure and lattice distortions on the magnetic properties of the low-index surfaces is also discussed.

II. THEORETICAL MODEL

Our calculations are based on the density functional theory using the projector-augmented wave (PAW) method and the generalized gradient approximation (GGA) as implemented in the Vienna *ab initio* simulation package (VASP).[20] We apply the Perdew-Burke-Ernzhof (PBE) functional for the exchange and correlation potentials.[21] For several calculations of bulk Mn_3N_2, the GGA + U approximation[22] was also employed, in these cases an effective on-site Coulomb $U = 3.9$ eV and exchange $J = 1$ eV energy corrections were applied to the Mn $3d$ orbitals.[23] These values have been used in previous calculations of MnN and (Ga,Mn)N alloys, and they correctly reproduce the thermodynamical stability of MnO and Mn_2O_3.[24–26]

Surfaces are modeled by periodically repeated slabs, containing between seven and thirteen atomic planes along the axis perpendicular to the surface and separated by a vacuum region larger than 11 Å. Symmetric slabs, with identical terminations at each side, were used for the surface calculations. The energy cutoff for the plane waves expansion of the electron wave function was set to 520 eV and the k-space sampling depends on the structure. All the calculations were performed with a Γ-centered mesh of equally spaced k points, an $8\times8\times2$ k mesh was chosen in the bulk Brillouin zone (BZ) and typically an $8\times8\times1$ mesh in the BZ of the slab modeling the surface calculations. The optimized structures are obtained by relaxing both, the cell and the internal coordinates until the convergence in the total free energy is better than 1 meV, the resulting forces acting on each atom never exceed 0.09 eV Å^{-1} and usually are smaller than 0.04 eV Å^{-1}. After relaxation the symmetric slabs remain invariant under reflection by the central plane, which always shows bulklike properties. Consequently, they equally model surfaces of either Mn_3N_2 single crystals or thin layers grown epitaxially as, for example, the Mn_3N_2 phase grown on MgO(001).[10,11] Convergence of the total energy and magnetic moments in the k sampling and the inclusion of relaxations were carefully checked, due to their prominent relevance for an accurate description of the magnetic configuration of the ground state.

The stability of a given Mn_3N_2 surface can be inferred from the surface energy, G_{sur}, which can be calculated from the total Gibbs free energy of a slab terminated in the corresponding surface and the Mn and N chemical potentials. Assuming that the surface is in thermodynamic equilibrium at temperature T and pressure P, neglecting the PV term—V is the volume—and taking the zero temperature limit, the surface energy G_{sur} of a symmetric slab containing N_{Mn} Mn and N_N N atoms and two identical surfaces at their boundaries, can be calculated by (see, e.g., Ref. 27 and references therein),

$$G_{\mathrm{sur}} = \tfrac{1}{2}\left(E^{\mathrm{tot}}_{\mathrm{slab}} - N_{\mathrm{Mn}}\,\mu_{\mathrm{Mn}} - N_{\mathrm{N}}\,\mu_{\mathrm{N}}\right), \tag{1}$$

where $E^{\mathrm{tot}}_{\mathrm{slab}}$ is the total energy of the slab and μ_{Mn} and μ_{N} the chemical potentials of manganese and nitrogen in the Mn_3N_2 compound, respectively. When the slab is stoichiometric, the last two terms correspond to an entire number of Mn_3N_2 units and thus N_{Mn} is a multiple of 3 and $N_{\mathrm{N}} = \frac{2}{3}\,N_{\mathrm{Mn}}$, then,

$$N_{\mathrm{Mn}}\,\mu_{\mathrm{Mn}} + N_{\mathrm{N}}\,\mu_{\mathrm{N}} = \tfrac{1}{3}\,N_{\mathrm{Mn}}\,\mu_{\mathrm{Mn_3N_2}}, \tag{2}$$

where $\mu_{\mathrm{Mn_3N_2}}$ is the chemical potential of a Mn_3N_2 nitride unit, which can be obtained from a bulk calculation.

Furthermore, for a nonstoichiometric Mn_3N_2 slab, taking advantage that the bulk Gibbs free energy $\mu_{\mathrm{Mn_3N_2}}$ can be expressed as

$$\mu^{\mathrm{bulk}}_{\mathrm{Mn_3N_2}} = 3\,\mu_{\mathrm{Mn}} + 2\,\mu_{\mathrm{N}} = 3\,g^{\mathrm{bulk}}_{\mathrm{Mn}} + g^{\mathrm{gas}}_{\mathrm{N_2}} + \Delta G^{f}_{\mathrm{Mn_3N_2}}, \tag{3}$$

where $g^{\mathrm{bulk}}_{\mathrm{Mn}}$ and $g^{\mathrm{gas}}_{\mathrm{N_2}}$ are the free energies of the Mn metal and nitrogen molecule, respectively, and $\Delta G^{f}_{\mathrm{Mn_3N_2}}$ is the heat of formation of the manganese nitride. The surface free energy becomes

$$G_{\mathrm{sur}} = \tfrac{1}{2}\left(E^{\mathrm{tot}}_{\mathrm{slab}} - \tfrac{1}{3}\,N_{\mathrm{Mn}}\,\mu_{\mathrm{Mn_3N_2}} - \left(N_{\mathrm{N}} - \tfrac{2}{3}\,N_{\mathrm{Mn}}\right)\mu_{\mathrm{N}}\right), \tag{4}$$

where the last term vanishes for stoichiometric systems [see Eq. (2)]. Therefore, for nonstoichiometric slabs the surface free energy is a linear function of the nitrogen chemical potential, μ_{N}, and thus it depends on the environmental conditions (i.e., N_2 pressure). G_{sur} is given by Eq. (4) and the range of μ_{N} allowed values is determined by the stability of the Mn_3N_2 compound,

$$\frac{\Delta G^{f}_{\mathrm{Mn_3N_2}}}{2} \leqslant \mu_{\mathrm{N}} - \frac{1}{2}\,g^{\mathrm{gas}}_{\mathrm{N_2}} \leqslant 0. \tag{5}$$

Otherwise, the manganese nitride would be unstable and would decompose into Mn metal and nitrogen. The surface free energy normalized by the cross-sectional area A, $\sigma = \frac{G_{\mathrm{sur}}}{2A}$, is used in the paper. It is independent of the two-dimensional surface unit cell, and then it allows one to determine the more stable surfaces and terminations.

III. ANTIFERROMAGNETIC BULK GROUND STATE

The Mn_3N_2 crystal corresponds to a tetragonally distorted rock-salt (RS) structure in which every third (001) plane does not contain N. The Mn_3N_2 lattice can be described, either as the face-centered tetragonal, fct, or the body-centered tetragonal, bct. In the present work, we use the fct description. The conventional fct unit cell is represented in Fig. 1. There are two inequivalent Mn atoms, Mn1 with only two N nearest neighbors in the adjacent planes along the (001) c axis and Mn2 with five N nearest neighbors, four within the plane and one in a nearest Mn-N (001) plane.

First, we investigate the ground state of bulk Mn_3N_2. Different collinear spin configurations of the magnetic moments localized in the Mn ions have been considered. Figure 2 shows the total energy as a function of the unit cell volume for various magnetic phases. Besides the ferromagnetic, FM, and the antiferromagnetic, AFM, states, two ferrimagnetic structures, FIM-21 and FIM-12, are presented. In all the configurations Mn spin moments align parallel within the (001) planes while the alignments between the (001) planes change

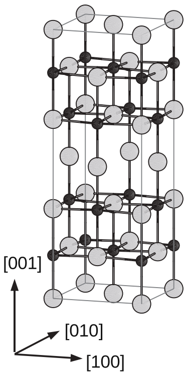

FIG. 1. Crystal structure of Mn_3N_2; gray large circles represent Mn atoms and small black circles represent N atoms.

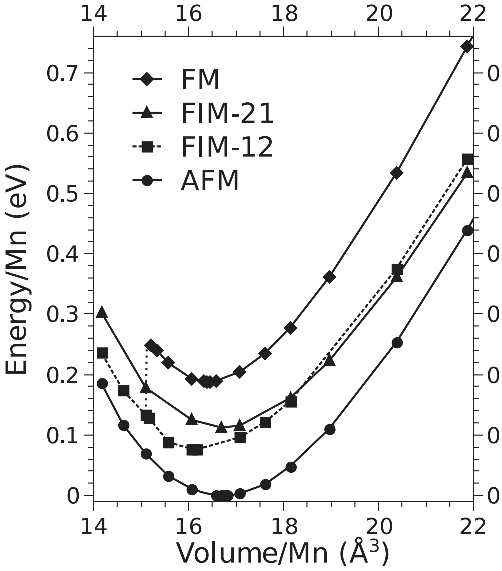

FIG. 2. Total energies as a function of the normalized volume per Mn atom for several spin configurations. Magnetic states are as follows: FM, ferromagnetic; AFM antiferrimagnetic; FIM-21 and FIM-12 correspond to the two ferrimagnetic states described in the text.

for the different phases:

$$\begin{aligned}&\text{AFM}\cdots\text{Mn1}\uparrow/\text{Mn2}\downarrow/\text{Mn2}\uparrow/\text{Mn1}\downarrow\cdots,\\&\text{FIM-21}\cdots\text{Mn1}\uparrow/\text{Mn2}\uparrow/\text{Mn2}\downarrow/\text{Mn1}\uparrow\cdots,\\&\text{FIM-12}\cdots\text{Mn1}\uparrow/\text{Mn2}\downarrow/\text{Mn2}\downarrow/\text{Mn1}\uparrow\cdots,\end{aligned}$$

The AFM configuration observed experimentally[1,2,4] is correctly predicted as the ground state for the complete explored volume range, even in the absence of Hubbard-like U corrections. The displayed energies correspond to calculations performed with the GGA approximation. The ordering of the equilibrium structures is $E_{AFM} < E_{FIM} < E_{FM}$. The FIM-12, FIM-21 and FM configurations at the equilibrium volumes are 76, 112, and 188 meV/Mn higher in energy, respectively. The same hierarchy is found in the GGA + U calculations, although the energy differences are larger, 102 and 278 meV/Mn for the FIM and FM ordering, respectively. The ferromagnetic structure is the most unfavorable and it undergoes a spontaneous transition to the FIM-12 solution for small volumes. Table I summarizes the structural parameters for the AFM equilibrium ground state. Experimental values and those obtained in previous calculations are also included. The agreement with the experimental values is very good although a slightly smaller and a larger lattice constant are obtained with the GGA and GGA + U approaches, respectively. Analogous behavior with respect to the exchange and correlation functionals has been found in calculations of the MnN bulk phase.[23] We found a c/a ratio in excellent agreement with the experiments. In perfect rock salt c/a takes the value 3. Thus, the calculated c/a reflects the distortion of the structure. The larger c/a deviation occurs for the AFM; we obtain $c/a = 2.96$ for the FM and 2.93 for the FIM configurations. This indicates that the compression of the c axis is a magnetic effect. Strain induced magnetically has also been predicted in MnN crystals.[19] For comparison the lattice parameters obtained within the LSDA approach for the fully relaxed bulk Mn_3N_2 in the AFM state[19] is also presented in Table I; those values are the smallest in the table.

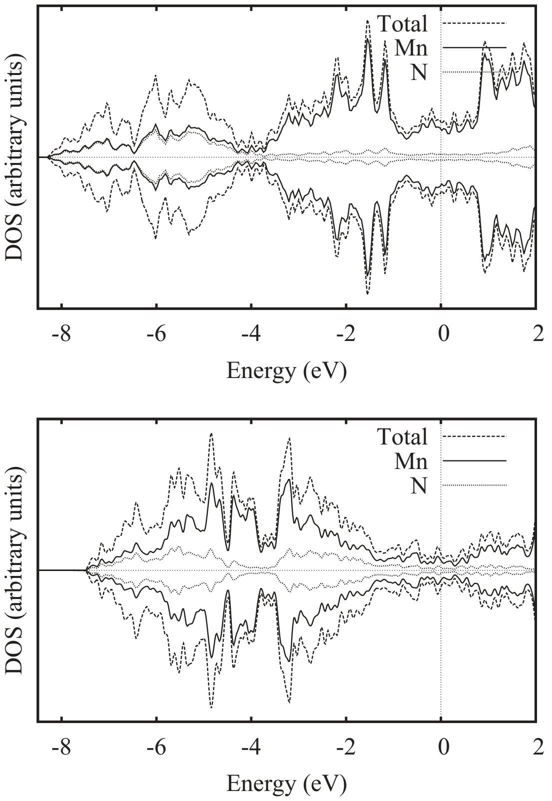

FIG. 3. Spin-resolved total density of states of AFM Mn_3N_2 and its decomposition in the Mn and N contributions, as predicted by GGA (top) and GGA + U (bottom). Positive (negative) values correspond to majority (minority) spin states. The energy zero is at the Fermi level.

TABLE I. Experimental and calculated fct lattice parameters (in Å) of bulk Mn_3N_2.

	Experiment					Theory		
	Ref. 1	Ref. 2		Ref. 3	Ref. 4	Ref. 19	This work	
		at 291 K	at 11 K			LSDA[b]	GGA[b]	GGA + U[b]
a	4.21[a]	4.20	4.19	4.23[a]	4.21	4.00[a]	4.10	4.30
c	12.13	12.13	12.10	12.50	12.12	11.52[a]	11.90	12.40
c/a	2.88	2.89	2.89	2.95	2.88	2.88	2.90	2.88

[a] Obtained from the reported bct lattice parameters.

[b] For the antiferromagnetic configuration.

The density of states (DOS) for the AFM spin configuration, decomposed into the atomiclike partial densities for the GGA and GGA + U calculations, are presented in Fig. 3. Both calculations predict a metallic state with the Fermi level (E_F) crossing the Mn 3*d* states. Below E_F, N 2*p*, and Mn 3*d* states dominate the valence band lower and higher energy regions, respectively. The effect of the on-site Coulomb interaction is to narrow the valence band and to increase the Mn exchange splitting, which result in stronger *p-d* hybridization. Nevertheless, the two approaches provide for the equilibrium structures, a qualitative analogous description of the system as a high-spin metallic state, similar to the previously reported LSDA results for the experimental unit cell volume.[19]

Due to the lack of cubic symmetry of the Mn_3N_2 crystal, its electronic states cannot be identified with the t_{2g} and e_g representations of the cubic lattice. The point group of the Mn_3N_2 crystal structure is the D_{4h}, a point group that possesses four one-dimensional even irreducible representations A_{1g}, A_{2g}, B_{1g}, and B_{2g} and a two-dimensional E_g representation. If the z axis is taken along the [001] direction—see Fig. 1—only the d_{xz} and d_{yz} orbitals, which belong to the E_g two-dimensional representation are equivalent. In fact, neither Mn nor N has octahedral coordination and the actual local symmetries are D_{4h} for the Mn1 and C_{4v} for the Mn2 and N lattice sites. For the D_{4h} group of the Mn1 site, the $d_{z^2-r^2}$ state transforms according to the full symmetry operations of the irreducible representation A_{1g}, while $d_{x^2-y^2}$ poses the B_{1g} symmetry; the d_{xy} orbital transforms according to B_{2g} and finally the orbitals $\{d_{xz},\, d_{yz}\}$ form the basis of the two-dimensional irreducible representation E_g. Similarly for the C_{4v} group of the Mn2 and N sites, $d_{z^2-r^2} \sim A_1$, $d_{x^2-y^2} \sim B_1$, $d_{xy} \sim B_2$, $\{d_{xz},d_{yz}\} \sim E$. Therefore, from symmetry arguments, only the d_{xz} and d_{yz} orbitals are equivalent. This is clearly seen in Fig. 4, which shows the orbital-projected density of states (PDOS) of the Mn1, Mn2, and N ions of bulk Mn_3N_2 in the antiferromagnetic configuration; GGA and GGA + U PDOS are presented. Since $d_{z^2-r^2}$ and $d_{x^2-y^2}$ are no longer equivalent, their PDOS differ considerably. The same is observed for the d_{xy} with respect to the PDOS of the d_{xz} and d_{yz} states. As previously discussed, both correlation and exchange functionals predict a high-spin metallic state, with the majority spin states completely occupied while the minority spin states are almost empty at each atomic site. Only a relevant occupation of the minority Mn1 $d_{x^2-y^2}$ orbital is obtained in the GGA calculation. The increase of the exchange splitting and consequently the enhancement of the N-Mn *p-d* coupling driven by the on-site Coulomb interaction, are clearly appreciated in the *d* Mn and *p* N states.

The calculated magnetic moments (*mm*) are, $mm_{\mathrm{Mn}_1} = 2.96\mu_B$ and $mm_{\mathrm{Mn}_2} = 3.03\,\mu_B$ in GGA and $mm_{\mathrm{Mn}_1} = 3.85\,\mu_B$ and $mm_{\mathrm{Mn}_2} = 4.07\,\mu_B$ in GGA + U, slightly larger in Mn2 than in Mn1. They are in reasonable agreement with the two possible sets of magnetic moments compatible with neutron scattering experiments, namely $mm_{\mathrm{Mn}_1} = 3.75(1)\,\mu_B$ and $mm_{\mathrm{Mn}_2} = 3.47(1)\,\mu_B$, or $mm_{\mathrm{Mn}_1} = 3.38(1)\,\mu_B$ and $mm_{\mathrm{Mn}_2} = 3.65(1)\,\mu_B$.[2,4] The GGA + U approach predicts larger magnetic moments of both Mn1 and Mn2. Notice that there is an ambiguity in the determination of the local moments, both experimental and theoretically. In particular, due to the difficulty in assigning the charge density to a given atom in a plane wave basis set method, the calculated values have to be considered qualitatively. Furthermore, our results compare reasonably with those previously reported,[16,19] although this calculation predicts slightly larger mm_{Mn1} than mm_{Mn2}.

The energy difference between the AFM and the higher energy magnetic configurations is large indicating a large stability of the AFM order. A mapping of the first-principles energy differences between different spin configurations to a Heisenberg Hamiltonian allows one to estimate the magnetic interactions between Mns. We found strong first-nearest-neighbor antiferromagnetic and second-nearest-neighbor ferromagnetic Mn-Mn exchange interactions in agreement with previous calculations.[19] Nevertheless, since the size of the magnetic moments depends on the magnetic configuration (see Table II), they might be considered as a rough approximation being consistent with a large Néel temperature.

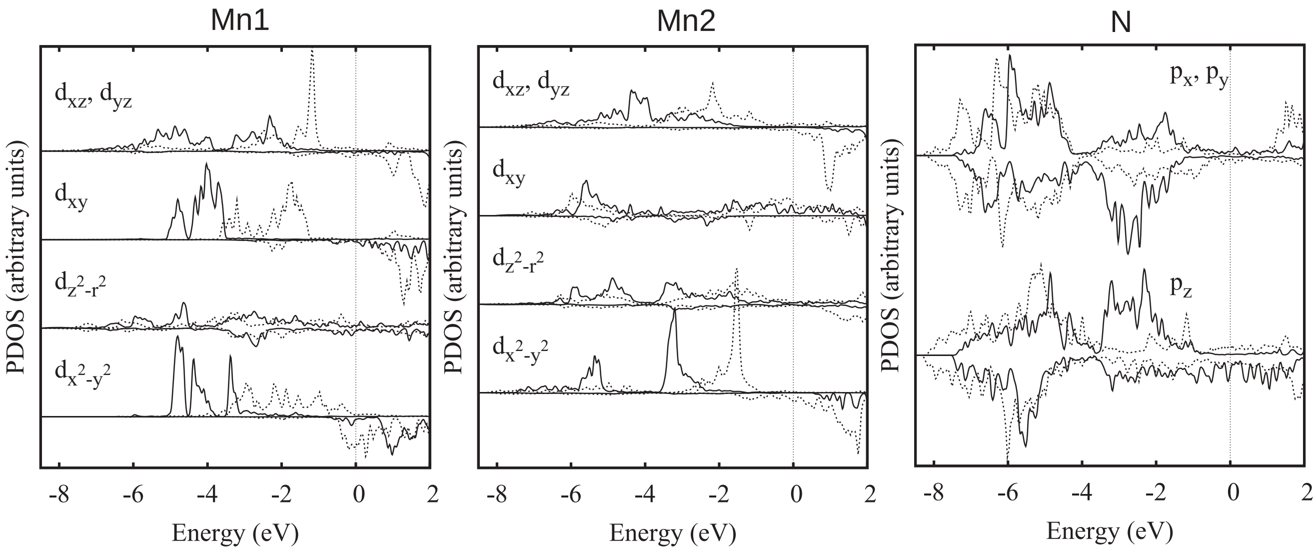

FIG. 4. Orbital decomposed atom resolved PDOS for AFM Mn_2N_3. Dashed lines correspond to GGA calculations and continuous lines to GGA + U. The energy zero is located at the Fermi level.

TABLE II. Composition, energy, and magnetization of the calculated (001), (010), and (110) slabs of Mn_3N_2. The deviation of the (001) slab from stoichiometry is indicated in the second row in parenthesis. The energies per Mn atom for the different magnetic configurations are referred to the energy of the AFM ground state. The values in parentheses to the right of the total magnetization correspond to the expected magnetization if the Mn in the slab maintain their bulk magnetic moments.

		Slabs (001)				
	Bulk[a]	Mn2-Mn1	Mn2-Mn2	Mn1-Mn2	Slab (010)	Slab (110)
N of atoms	10	15	19	21	70	65
N of Mn1	2	3	3 (-1)	5 (+1)	14	13
No. of Mn2	4	6	8	8	28	26
No. of N	4	6	8	8	28	26
E_{FIM} (in meV)	76	45	94	61	65	63
E_{FM} (in meV)	189	180	162	172	191	177
Magnetization (in μ_B)	AFM					
$\|mm_{Mn_1}\|$	2.96	2.78[c]	2.93[d]	3.69[b]	3.30,[b] 2.93[c]	3.24,[b] 3.05[c]
$\|mm_{Mn_2}\|$	3.03	3.03,[b] 2.87[d]	3.17,[b] 2.85[c]	2.86,[c] 3.00[d]	3.40,[b] 2.84[c]	3.25,[b] 2.53[c]
Total	0.00	3.45 (3.11)	3.84 (2.96)	5.56 (2.96)	0.00 (0.00)	13.27 (9.02)
	FIM					
$\|mm_{Mn_1}\|$	2.88	2.82[c]	2.73[d]	3.61[b]	3.11,[b] 2.67[c]	2.75,[b] 2.93[c]
$\|mm_{Mn_2}\|$	2.61	2.96,[b]2.53[d]	3.24,[b] 2.46[c]	2.57,[c] 2.53[d]	3.36,[b] 2.52[c]	3.10,[b] 2.38[c]
Total	4.83	8.09 (7.24)	14.37 (12.5)	4.71 (6.8)	39.61 (33.81)	33.22 (31.39)
	FM					
mm_{Mn_1}	2.79	2.36[c]	2.87[d]	3.65[b]	2.69,[b] 2.60[c]	2.68,[b] 2.84[c]
mm_{Mn_2}	2.64	2.81,[b] 2.57[d]	3.25,[b] 2.46[c]	2.71,[c] 2.64[d]	2.84,[b] 2.50[c]	2.72,[b] 2.31[c]
Total	16.44	23.90 (24.66)	31.40 (29.9)	38.49 (35.7)	113.33 (115.08)	105.36 (106.87)

[a] Calculated for the bct structure.
[b] 1st atomic layer (surface).
[c] 2nd atomic layer.
[d] 3rd atomic layer.

Finally, the detailed inspection of the relaxed structures, energies, partial charges, and magnetizations obtained within the GGA and GGA + U shows that both approaches provide qualitatively similar results for the Mn_3N_2 bulk crystal. Hence, in the rest of the paper we mostly discuss results obtained with the spin-polarized PBE GGA approach.

IV. (001) SURFACES

First we investigate the Mn_3N_2 (001) surfaces. Along the [001] direction two Mn2N planes alternate with a Mn1 plane noncontaining N. Thus, there are three possible inequivalent terminations, hereafter labeled Mn2-Mn1, Mn2-Mn2, and Mn1-Mn2, where the first and second type of Mn correspond to those at the surface and the subsurface layer, respectively. Figure 5 shows the relaxed structures for the three terminations. All the surfaces present a corrugation of the Mn2N layers, with the surface N shifted outward. The relaxation is not restricted to the first Mn2N plane but extends towards the center of the slab. However, while in the first Mn2N plane N always move outwards the surface in the layers underneath the bulk pattern is followed. In fact, in bulk, N atoms in Mn2N layers are also slightly shifted from the Mn fct positions towards the Mn1 planes. Moreover, the corrugation is larger at the surface particularly in the case of Mn2-terminated ones. N moves 0.12 Å in the first and second layer of the Mn2-Mn1 and 0.13 and 0.15 Å in those of the Mn2-Mn2 surfaces as compared with the 0.07 Å in bulk. Nevertheless, the changes of bond distances and angles associated with corrugation do not alter the coupling of the Mn moments, which remains FM within the [001] planes and AFM between consecutive [001] layers.

In order to have symmetric slabs with the same termination at both ends, the thickness of the slabs modeling the three (001) surfaces was different, namely 9, 11 and 13 atomic layers for the Mn2-Mn1, Mn2-Mn2, and Mn1-Mn2, respectively. After relaxation, we obtain for the corresponding slabs, *in-plane* lattice parameters very close to the 4.10 Å bulk value, but slightly smaller 4.04, 4.06, and 4.09 Å, respectively. There is also a slight *out-of-plane* lattice expansion, 4.05 Å (Mn2-Mn1), 4.02 (Mn2-Mn2), and 3.99 Å (Mn1-Mn2) compared with the 3.974 Å in bulk. The evolution of the lattice parameters correlates with the number of layers. For thin slabs the surface expansion dominates and gives rise to a slight increase of the *out-of-plane* lattice parameter, which, however, approaches quickly the bulk value. In addition, the *in-plane* lattice parameters behave opposite and the volume is preserved, indicating that the elastic energy determines the slab relaxation. Similar behavior has been observed experimentally since there is almost no change between the lattice parameters of the bulk and those measured in $\eta_\perp$ (001) Mn_3N_2 films grown epitaxially on MgO (001) substrate. Only a very small increase of the *in-plane* lattice parameter is seen for increasing film thicknesses.[29] However, some dispersion exists in the experimentally reported c parameters, which range from 12.24 to 12.12 Å, probably due to the deviation of $\eta_\perp$ films from

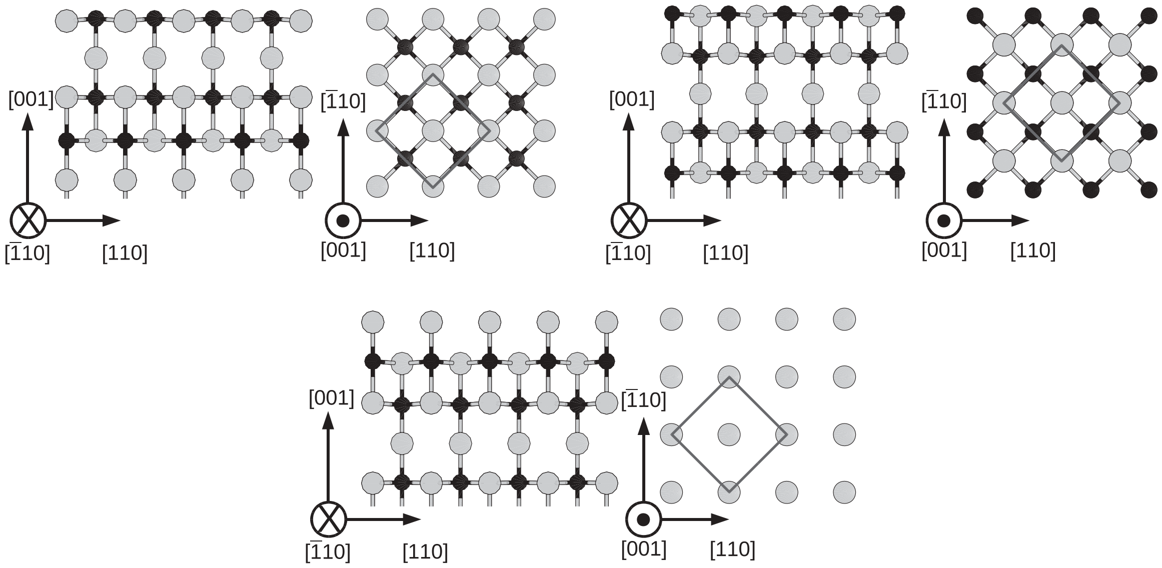

FIG. 5. Calculated relaxed atomic structure for the tree possible terminations of the (001) surface: Mn2-Mn1, Mn2-Mn2, and Mn1-Mn2 from left to right and from top to bottom. See text for the explanation of the notations of different structures. Side view and top view are represented at the left and right of each figure, respectively. The side views include the five atomic planes closest to the surface, while the top views include only atoms in the first surface plane. The two-dimensional unit cells are indicated in the top views. Mn atoms are represented by large gray and N atoms by small black circles.

stoichiometric Mn_3N_2, being its composition close to the Θ-MnN phase.[11,15]

In addition to the structural changes, there is an enhancement of the surface magnetization; (001) surfaces and thin films are ferrimagnetic systems, despite the AFM coupling between layers. The net magnetization differences are given in Table II. The Mn1 termination presents the largest net magnetization; Mn1 in the surface has only a bond to N and then Mn is close to the high-spin atomiclike configuration. The net magnetization of Mn2-terminated surfaces is smaller and only a moderate increase of the surface magnetic moments is predicted. Unexpectedly larger values are obtained for the Mn2-Mn2 than for the Mn2-Mn1 termination, despite the fact that Mn2 on the former surface has the same coordination and local environment as that in the bulk. In fact the net magnetization has its origin not only in the surface Mn but in all the adjacent atoms. The surface induced effects are also appreciated in the atom projected density of states. The orbital decomposed PDOS of the surface Mn is presented in Fig. 6 for the three terminations. The existence of unsaturated bonds in all the surfaces is clearly seen in the orbitals with the z component, and is specially important for the $d_{z^2-r^2}$ orbital of

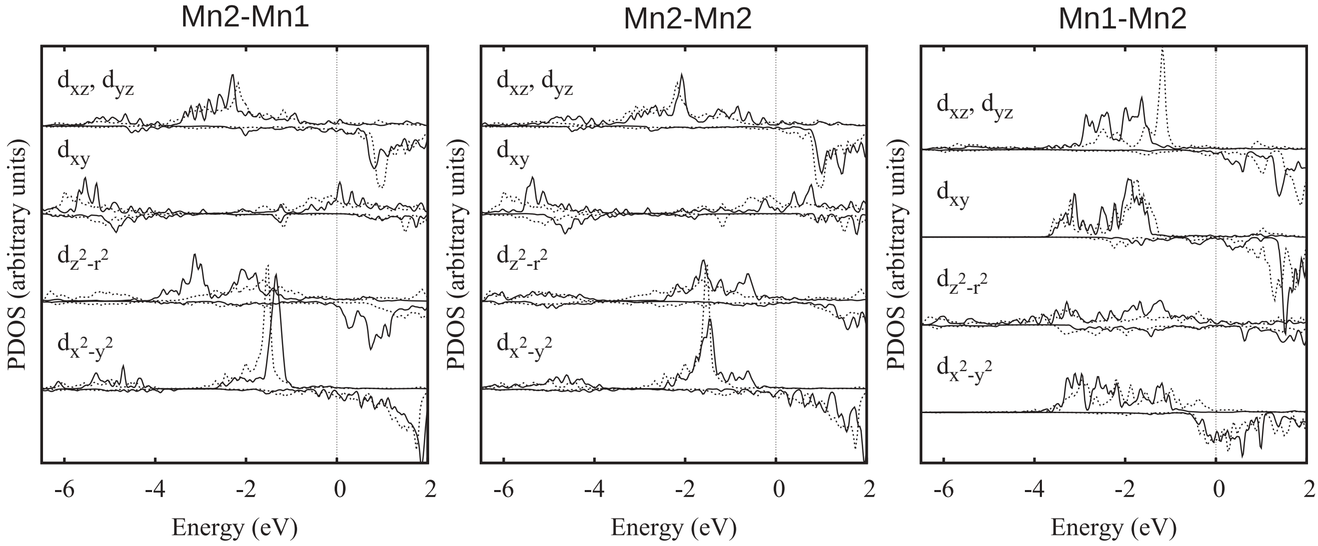

FIG. 6. Orbital decomposed PDOS for the surface Mn of the three inequivalent surface terminations, from left to right: Mn2-Mn1, Mn2-Mn2, and Mn1-Mn2, respectively. Continuous lines are PDOS for the surface Mn and dashed lines are those of the corresponding bulk Mn. The energy zero is located at the Fermi level.

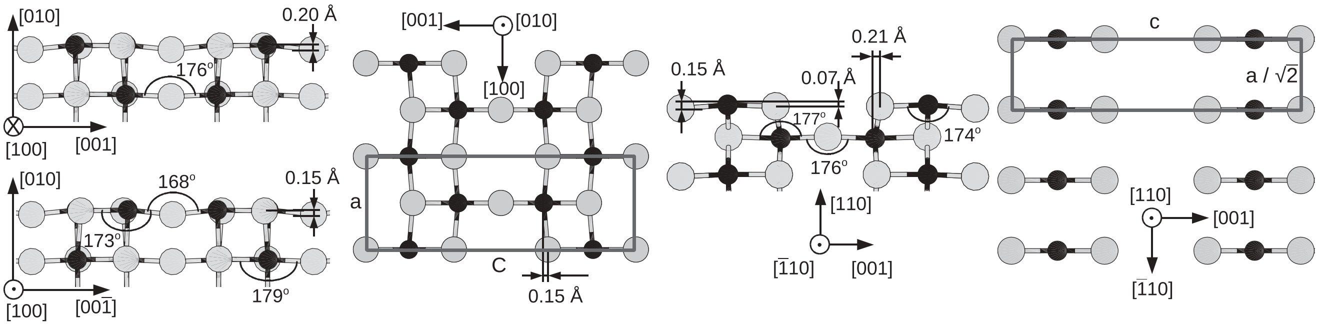

FIG. 7. Same as Fig. 5 for the (010) (left) and (100) (right) surfaces.

the Mn2-Mn2 surface. In this surface, two bonds, one of Mn and one of N are unsaturated. Nevertheless, the N-Mn *p-d* hybridization dominates the low energy region and thus, the existence of unsaturated bonds does not affect substantially the total magnetization. Narrowing of the surface bands and changes in the DOS are more relevant in the Mn1-Mn2 surface in agreement with its large spin polarization.

V. (010) AND (110) SURFACES

Mn_3N_2 thin films epitaxially grown on MgO (001) substrates show, besides the previously discussed (001) Mn2 termination, domains compatible with the (010) surface, that is, with the c axis parallel to the growth surface. Neutron scattering of slabs grown on the (010) direction indicates their layerwise AFM bulk magnetic structure, which results in an AFM surface.[10] In fact, atomic-scale spin-polarized scanning tunneling microscopy demonstrates the unique row-wise AFM spin structure of this surface,[12,14,16,17] since simulations of the SP-STM experiments based on spin-polarized DFT calculations of the (010) surface corresponding to the cleaved bulk Mn_3N_2 crystal show good agreement with the observed bias-dependent behavior. Nevertheless, the equilibrium surface structure has not been calculated and there is not information about the surface magnetic moments.[12,14,16,17]

Figure 7 represents the geometrical structure of the calculated equilibrium (010) surface, which contains the two types of manganese atoms, Mn1 and Mn2, with two and three in-plane bonds to N, respectively. Along the [001] direction the surface consists of rows of Mn1 alternating with two Mn2, the distance between two equivalent rows is $c/2$, corresponding to the spacing between planes of nitrogen vacancies in the bulk. The (010) equilibrium surface presents a distorted bulklike structure. The larger effect is the corrugation of about 0.15–0.20 Å of the Mn1 and Mn2 sublattices and also an 0.15-Å in-plane lattice distortion of the Mn2-N position is observed. The corrugation is of the same order that the measured height difference of about 0.08 Å between Mn1 and Mn2 atoms in atomic resolved STM images, for bias voltages in the range of $+0.6 \leqslant V_S \leqslant -0.7$ V, which was attributed to surface relaxation.[13]

The surface is metallic with Mn states at the Fermi level, in agreement with the observed metallic behavior.[12] The lattice distortions result in a variation of bond angles—see Fig. 7—which however do not influence greatly the magnetic coupling, therefore the surface presents a row-wise AFM spin structure. Magnetic moments are enhanced at the surface and the calculated values are $mm_{\mathrm{Mn}_1} = 3.30$ and $mm_{\mathrm{Mn}_2} = 3.40\ \mu_{\mathrm{B}}$, which compare, respectively, with the 2.96 and 3.03 bulk moments (see Table II). Nevertheless, as a result of the AFM coupling within each layer the total magnetization is zero.

Turning now to the (110) surface, Fig. 7 also shows its equilibrium structure. Although Mn1 and Mn2 atoms are located on the top plane, this surface differs drastically from all the other low-index surfaces. Structurally, it contains rows along the [001] direction, the transversal unit in the surface layer is formed by an Mn1 in the center and two Mn2 at each edge separated by N, and the row spacing corresponds to the nitrogen vacancies distance c. Analogous to the (010) surface there is a buckling, but in this case all the Mn atoms shift inwards to the surface and Mn-N-Mn angles deviate slightly from the bulk 2π value. Moreover, all Mn atoms on the surface are FM coupled while there is AFM coupling between nearest-neighbor atomic planes, analogously to the (001) surface terminations. This results in a peculiar spin configuration with FM ribbons separated by an empty channel with a Mn1 AFM coupled in the layer underneath. Surface magnetic moments are enhanced and they take the value of 3.25 μ_B independent of the type of Mn.

VI. MAGNETIC ENERGIES AND SURFACE STABILITY

The discussed surfaces correspond to the magnetic ground states. Our calculations indicate that all the surfaces follow the layerwise AFM bulk magnetic structure and thus their spin configurations are those of ideal bulk terminations. All the terminations of the (001) surfaces are ordinary AFM layered systems, with all the spin in a plane coupled ferromagnetically. In contrast the (010) and (110) surfaces present unique spin configurations with singular one-dimensional structures, while in the former AFM rows alternate along the [001] direction in the latter FM ribbons separated by an atom thick empty row extending along the [$\bar{1}$10] direction.

We have explored several ferrimagnetic collinear phases and their energies are always higher than the energy of the derived bulklike AFM states. Table II compares the energies for the ferromagnetic and the ferrimagnetic configuration labeled FIM-12 in Sec. III for all the low-index surfaces. Energies are given with respect to that of the ground state. The higher energies correspond to the ferromagnetic configuration; they are slightly dependent on the surface and similar to the bulk values. Opposite, a large dispersion is obtained for the FIM-12 states, which show a surface dependence, although except for the unstable Mn1-Mn2 surface, the energy differences with the ground state are smaller for the surface than in the bulk. Therefore, bulk and surfaces show similar ordering of the spin configurations, supporting the cleaved bulklike magnetic properties of low-index Mn_3N_2 surfaces. The main effect of the surface is to enhance the *mm* of the topmost atoms, which are also shown in Table II. All these results indicate that the broken symmetry induced by the surface does not alter drastically the competition between indirect FM Mn-N-Mn and direct AFM Mn-Mn exchange interactions determining the bulk spin configuration.

As explained previously, by combining first-principles calculations and a thermodynamic approach it is possible to calculate the surface energy. Their comparison for different surfaces allows one to discuss their thermodynamic stability and to predict the more stable surface. We follow the procedure described in Sec. II and calculate the surface energy for the different terminations as a function of the nitrogen chemical potential, μ_N, by Eqs. (1)–(4). The value of μ_N is bounded between the chemical potential of the N_2 molecule $g_{N_2}^{gas}$ and the heat of formation per formula unit of Mn_2N_3, which takes the value $\Delta G^f_{Mn_3N_2} = -1.519$ eV[28] [see Eq. (5)]. E^{tot}_{slab} and $\mu_{Mn_3N_2}$ are the results of the slab and bulk calculations, respectively. The surface energies for the different (001) terminations as a function of μ_N are represented in Fig. 8. The slabs modeling the Mn2-Mn2 and Mn1-Mn2 surfaces are nonstoichiometric, thus their surface energies depend on μ_N and consequently on the nitrogen atmosphere. The Mn2-Mn1 is the most stable termination for small N chemical potentials or equivalently under N-poor conditions (points on the left ordinate axis in Fig. 8). As the μ_N increases the difference between Mn2-Mn1 and Mn2-Mn2 decreases and for N-rich conditions the Mn2-Mn1 termination is the most stable. Nevertheless, since their difference is small our calculations show that the Mn2 surface terminations are relatively insensitive to variations in the chemical conditions of the environment. This result corroborates the experimental findings, surfaces terminated in Mn2N planes have been observed experimentally[10–15] and both terminations have been proposed to explain the STM images of Mn_3N_2 thin films.[15] The Mn1-Mn2 (001) termination has a larger surface energy and thus it is unlikely to be formed in slabs grown in the [001] direction, its large σ may account for the observed Mn tetramer reconstruction observed in this surface. However, we have also investigated the Mn1 tetramer reconstruction and found that it is not energetically favorable; even more when allowed to relax it reverts to the 1 × 1 structure, which is energetically more stable.

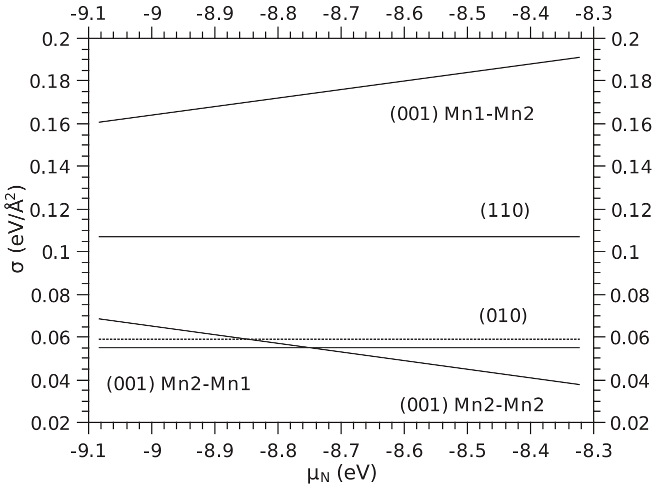

FIG. 8. Calculated energies of the low-index Mn_3N_2 surfaces as a function of N chemical potential. See text for the explanation of the notations for different structures.

The formation energies of the (010) and (110) surface are also presented in Fig. 8. In both surfaces all the atomic planes are stoichiometric and then surface energies do not depend on the N chemical potential. The energy of the (010) surface is slightly larger than those of the Mn2 surfaces, but the energy difference is quite small and therefore the growth of this surface is quite likely to occur, which explains the growth of both (001) and (010) Mn_3N_2 films on (001) MgO under similar growth conditions.[10,15] On the other hand, the energy difference with the (110) although larger is not large enough to exclude their formation $\sigma \sim 100$ meV/Å. Thus, it appears that the (110) termination, with a singular magnetic configuration due to its FM ribbon structure, is plausible to stabilize.

VII. CONCLUSIONS

We have investigated the low-index surfaces of Mn_3N_2 using the density-functional formalism. Bulk calculations indicate that both, GGA and GGA + U correlation and exchange functionals correctly predict the experimentally observed AFM ordering along the [001] direction and the metallic character of Mn_3N_2 crystals. The low-index surfaces correspond to the distorted cleaved bulk crystal and surface corrugation and buckling are predicted in almost all the surfaces. However, despite the structural lattice distortions the surface magnetic configurations are those obtained from the layerwise AFM bulk structure. The ferromagnetic (001) Mn2 termination and the row-wise AFM (010) surfaces observed experimentally are found to be thermodynamically most stable. In addition, the FM (110) surface with a singular ribbonlike modulated structure, seems to be plausible to stabilize, since its surface energy is only ∼50 meV/Å above the more stable (001) surface. The electronic structure of all the low-index Mn_3N_2 surfaces is consistent with a metallic state. The Fermi level is mostly dominated by Mn minority spin electrons, whereas majority states are fully occupied. Bonding Mn-N states have energies in the lower part of the valence band and thus broken bonds at the surface do not alter drastically the spin configuration although an enhancement of the Mn and induced N magnetic moments is produced in all the surfaces. Our results indicate that ferromagnetism observed in $Ga_{1-x}Mn_xN$ is unlikely due to the formation of Mn_3N_2 precipitates.

ACKNOWLEDGMENTS

This work has been partially supported by the Spanish CSIC Intramural Project No. 201060E041, and by the Spanish Ministry of Science and Technology (MICI) under Grant No. MAT2009-14578-C03-03. Part of the computations were performed at the Supercomputing Centre of Galicia (CESGA).

[*] mcarmen@icmm.csic.es

[1] H. Jacobs and C. Stüve, J. Less-Common Met. **96**, 323 (1984).

[2] G. Kreiner and H. Jacobs, J. Alloys Compd. **183**, 345 (1992).

[3] M. Hasegawa and T. Yagi, J. Alloys Compd. **403**, 131 (2005).

[4] A. Leineweber, R. Niewa, H. Jacobs, and W. Kockelmann, J. Mater. Chem. **10**, 2827 (2000).

[5] M. van Schilfgaarde and O. N. Mryasov, Phys. Rev. B **63**, 233205 (2001).

[6] Y. Liu, L. Xu, X. Li, P. Hu, and S. Li, J. Appl. Phys. **107**, 103914 (2010).

[7] E. Céspedes, Y. Huttel, L. Martinez, A. de Andrés, J. Chaboy, M. Vila, N. D. Telling, G. van der Laan, and C. Prieto, Appl. Phys. Lett. **93**, 252506 (2008).

[8] E. Céspedes, E. Róman, Y. Huttel, J. Chaboy, J. García-Lopez, A. de Andrés, and C. Prieto, J. Appl. Phys. **106**, 043912 (2009).

[9] M. Tabuchi, M. Takahashi, and F. Kanamaru, J. Alloys Compd. **210**, 143 (1994).

[10] H. Yang, H. Al-Brithen, A. Smith, J. A. Borchers, R. L. Cappelletti, and M. D. Vaudin, Appl. Phys. Lett. **78**, 3860 (2001).

[11] H. Yang, H. Al-Brithen, E. Trifan, D. C. Ingram, and A. R. Smith, J. Appl. Phys. **91**, 1053 (2002).

[12] H. Yang, A. R. Smith, M. Prikhodko, and W. R. L. Lambrecht, Phys. Rev. Lett. **89**, 226101 (2002).

[13] H. Yang, R. Yang, A. R. Smith, and W. R. L. Lambrecht, Surf. Sci. **548**, 117 (2004).

[14] A. R. Smith, R. Yang, H. Yang, W. R. L. Lambrecht, A. Dick, and J. Neugebauer, Surf. Sci. **561**, 154 (2004).

[15] R. Yang, M. B. Haider, H. Yang, H. Al-Brithen, and A. R. Smith, Appl. Phys. A **81**, 695 (2005).

[16] A. R. Smith, R. Yang, H. Yang, A. Dick, J. Neugebauer, and W. R. L. Lambrecht, Microscopy Research Technique **66**, 72 (2005).

[17] R. Yang, H. Yang, A. R. Smith, A. Dick, and J. Neugebauer, Phys. Rev. B **74**, 115409 (2006).

[18] K. Wang and A. R. Smith, Nanoletters (2012), doi:10.1021/n1204192n.

[19] W. R. L. Lambrecht, M. Prikhodko, and M. S. Miao, Phys. Rev. B **68**, 174411 (2003).

[20] G. Kresse and J. Hafner, Phys. Rev. B **47**, 558 (1993); G. Kresse and J. Furthmüller, *ibid.* **54**, 11169 (1996); G. Kresse and D. Joubert, *ibid.* **59**, 1758 (1999).

[21] J. P. Perdew, K. Burke, and M. Ernzerhof, Phys. Rev. Lett. **77**, 3865 (1996); **78**, 1396 (1997).

[22] A. I. Liechtenstein, V. I. Anisimov, and J. Zaanen, Phys. Rev. B **52**, R5467 (1995); F. A. Vladimir, I. Anisimov, and A. I. Lichtenstein, J. Phys.: Condens. Matter **9**, 767 (1997).

[23] J. A. Chan, J. Z. Liu, H. Raebiger, S. Lany, and A. Zunger, Phys. Rev. B **78**, 184109 (2008).

[24] S. Lany, H. Raebiger, and A. Zunger, Phys. Rev. B **77**, 241201(R) (2008).

[25] B. Sanyal, O. Bengone, and S. Mirbt, Phys. Rev. B **68**, 205210 (2003).

[26] L. M. Sandratskii, P. Bruno, and J. Kudrnovsky, Phys. Rev. B **69**, 195203 (2004).

[27] J. I. Beltrán Fínez, Ph.D. thesis, Universidad Autonoma de Madrid, 2006.

[28] S. H. Elder, F. J. DiSalvo, L. Topor, and A. Navrotsky, Chem. Mater. **5**, 1545 (1993).

[29] R. Yang, Ph.D. thesis, Ohio University, 2006.